communications earth & environment

A Nature Portfolio journal

Article

https://doi.org/10.1038/s43247-026-03227-2

Igneous and sedimentary origins of Jezero crater units from X-ray crystal mapping on Mars

Check for updates

Brendan J. Orenstein[1,2], **David T. Flannery**[1,2] ✉, **Michael W. M. Jones**[2,3,4], **Eleanor L. Moreland**[5], **Kirsten L. Siebach**[5], **Michael M. Tice**[6], **Allan H. Treiman**[7], **Briony Horgan**[8], **Balz Kamber**[1], **Athanasios Klidaras**[8], **Luke Nothdurft**[1,2], **Yang Liu**[9], **Edward A. Cloutis**[10], **Abigail C. Allwood**[9] & **Scott VanBommel**[11]

Jezero crater is located in Mars' largest olivine-rich region, which is variously interpreted as lava flows, intrusive plutons, clastic sediments, or pyroclastics. In Jezero crater, several olivine-rich units have been investigated by the *Perseverance* rover, including an olivine cumulate in the crater floor (Séítah formation) and the enigmatic "Margin Unit"; an olivine- and carbonate-rich unit commonly interpreted as either a lake shore deposit or a local expression of the regional olivine-carbonate unit. We developed a method incorporating X-ray diffraction energy and spatial information to accurately determine the forsterite content (molar percentage of MgO/(MgO+FeOT)) of monocrystalline olivine encountered by *Perseverance*. Forsterite content in clastic sediments of the western Jezero fan indicate multiple olivine sources. In contrast, forsterite content analysed in the Margin Unit is similar to the Séítah formation, suggesting that at least some of the Margin Unit may represent an altered igneous cumulate with similar origins to the Séítah formation.

The southwestern rim of the ~3.96 Ga[1] Isidis Planitia impact basin and the Nili Fossae area hosts one of the most expansive olivine-rich deposits on Mars[2,3] (Fig. S1). This area is also unique for preserving regionally-extensive magnesium carbonate and large (mm-sized) olivine grains[3,4]. The olivine has been attributed to impact-related melting/intrusive volcanism[2,5,6], lava flows[3,7], clastic sedimentary[8] and/or explosive volcanic processes[9,10], with carbonate addition via hydrothermal alteration or surface weathering of mafic minerals[4,11–14] and possibly with a contribution from direct precipitation of carbonate in ephemeral lakes[15].

Since the Mars 2020 *Perseverance* rover landed in Jezero crater in 2021, it has traversed, analysed, and sampled olivine in aqueously altered igneous rocks in the crater floor (Séítah and Máaz formations), in clastic rocks in the fan cropping out on the western edge of the crater (Tenby and Otis Peak formations), and in enigmatic rocks outcropping along the western margin of the crater (the Margin Unit). Elemental chemistry measurements have been performed by SuperCam via Laser Induced Breakdown Spectroscopy (LIBS)[16,17], as well as by the Planetary Instrument for X-ray Lithochemistry (PIXL); a micro-X-ray fluorescence (XRF) spectrometer mounted to *Perseverance's* robotic arm[18]. Fluoresced X-rays detected by PIXL are used to generate quantitative elemental abundance maps, typically of cm-sized regions exposed by the rover's abrasion tool[19]. X-ray diffraction peaks are also present in PIXL's XRF spectra[20,21], allowing PIXL to acquire co-located elemental and crystallographic information[20,22–26]. PIXL data can be co-registered with images for expanded spatial context, such as the PIXL Micro-Context Camera (MCC)[18], close up images from the Wide Angle Topographic Sensor for Operations and eNgineering (WATSON), and Autofocus Context Imager (ACI) cameras mounted to the rover's robotic arm[27]. Additional context is provided by navigation cameras (Navcam) and hazard avoidance cameras (Hazcam)[28].

---

[1]School of Earth and Atmospheric Sciences, Queensland University of Technology, Brisbane, QLD, Australia. [2]Centre for Planetary Surface Exploration, Queensland University of Technology, Brisbane, QLD, Australia. [3]Central Analytical Research Facility, Queensland University of Technology, Brisbane, QLD, Australia. [4]School of Chemistry and Physics, Queensland University of Technology, Brisbane, QLD, Australia. [5]Department of Earth, Environmental and Planetary Sciences, Rice University, Houston, TX, USA. [6]Department of Geology and Geophysics, Texas A&M University, College Station, TX, USA. [7]Lunar and Planetary Institute, Universities Space Research Association, Houston, TX, USA. [8]Department of Earth, Atmospheric, and Planetary Sciences, Purdue University, West Lafayette, IN, USA. [9]Jet Propulsion Laboratory, California Institute of Technology, Pasadena, CA, USA. [10]Department of Geography, University of Winnipeg, Winnipeg, MB, Canada. [11]Department of Earth, Environmental and Planetary Sciences, Washington University in St. Louis, St. Louis, MO, USA.
✉e-mail: david.flannery@qut.edu.au

Olivine fosterite content (Fo-content, defined here as the molar percentage of MgO/(MgO+FeO_T)) is a useful indicator of the magnesium to iron ratio in melts[29] and therefore clast provenance[30]. However, inaccurate mineral quantifications can occur due to contributions from surrounding mineral phases (particularly Si, Fe, or Mg rich phases) in a process known as beam mixing[26,31], leading to inaccurate Fo-content results. Ideally, measurements should be limited to individual grains to reduce the effects of beam mixing; however, tool marks left by the abrasion bit obscure grain extents, making visual identification of grain boundaries unreliable[32] and hindering accurate mineral chemistry. Previously, the effects of beam mixing on PIXL measurements have been reduced through processes such as mineral stripping[26] and compositional deconvolution into mineral endmembers[31]. These methods require significant user input[31], making their general application difficult and subject to user error, limiting their application.

Here, we extended the diffraction mapping technique developed by Orenstein et al.[23] and combined it with data from the Mineral Identification by SToichiometry (MIST) algorithm[33] to identify and investigate elemental variations across populations of olivine crystals with reduced contamination from surrounding minerals. This combination of PIXL elemental and diffraction data allows us to accurately map the Fo-content without contamination from surrounding material in abrasion patches collected during the first 1153 sols of the mission, revealing distinct olivine populations for each of *Perseverance's* science campaigns.

Perseverance's traverse

Perseverance performed four science campaigns during the first 1153 sols of the Mars 2020 mission; the crater floor campaign (sols 100–379)[34], the fan front campaign (sols 410–709)[35], the upper fan campaign (sols 708–910)[36–38], and the Margin Unit campaign (beginning sol 910)[36,39], with crystalline olivine observed in abrasion patches in all campaigns except for the fan front (Fig. 1). During these campaigns SuperCam LIBS detected olivine Fo-content between ~50 and ~80[40]. This spans a similar Fo-content range from Martian meteorite classes (except for nakhlites and augite-rich shergottites)[40,41], orbital measurements conducted prior to landing (Fo-content between 60 and 70)[2], and results from the *Curiosity* rover at Gale crater, where Fo-content between 60 and 72 was determined for fluvio-lacustrine samples and between 54 and 60 for igneous samples[42].

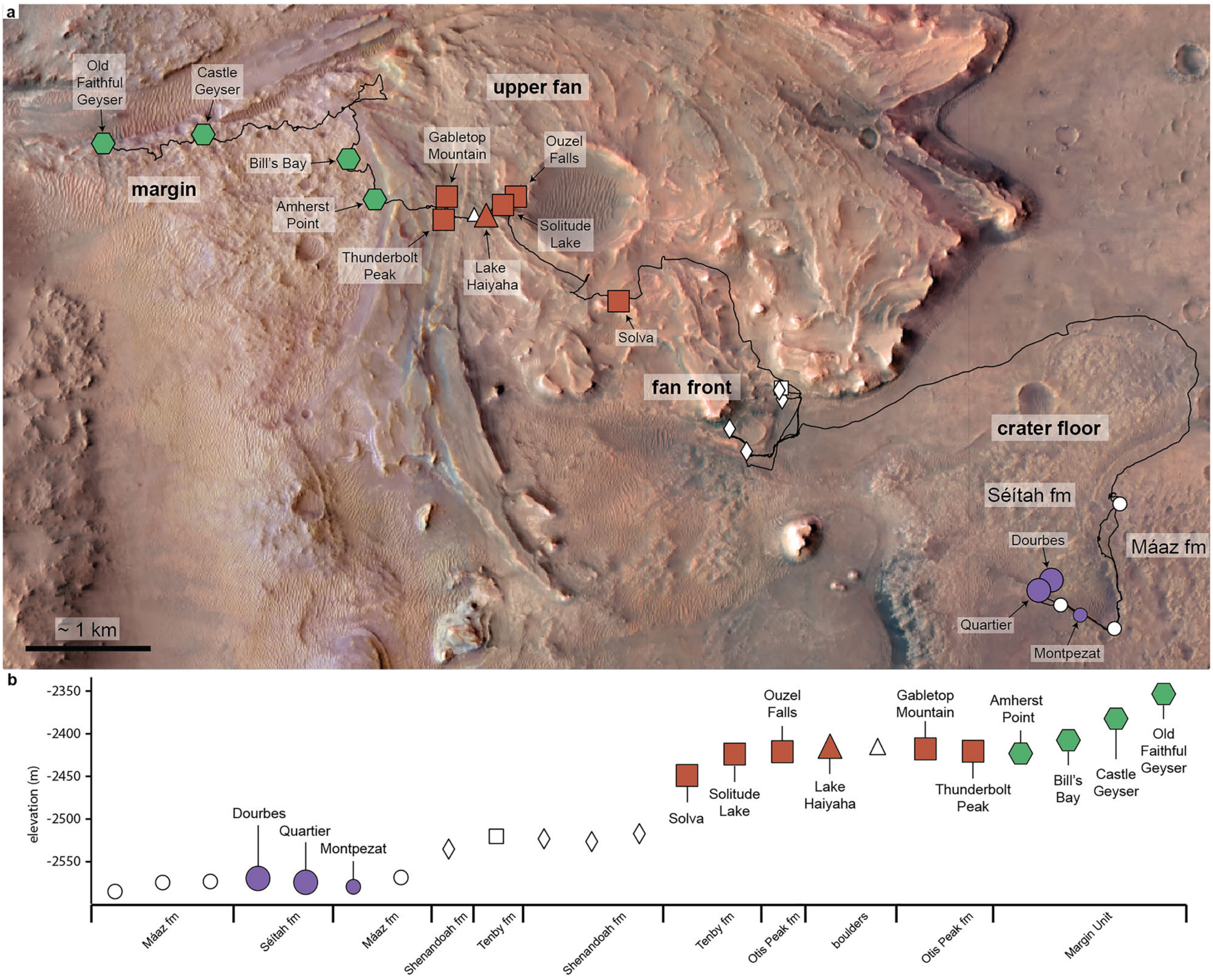

Fig. 1 | Orbital context image showing the *Perseverance* rover traverse and locations of monocrystalline olivine in abrasion targets in Jezero crater, and elevations and geological units for the studied abrasion patches. a Orbital context image showing the *Perseverance* rover traverse and locations of monocrystalline olivine in abrasion targets in Jezero crater. See Table S4 for image source. **b** Elevations and geologic units for the studied abrasion patches. Circles correspond to the crater floor, diamonds to the fan front, squares to the upper fan, triangles to float boulders in the upper fan and hexagons to the Margin Unit. Larger coloured markers correspond to abrasions with olivine identified by MIST in spatially coherent monocrystalline regions, smaller coloured markers correspond to abrasions without MIST identified olivine in spatially coherent monocrystalline regions (Table 1). A single colour is given to each science campaign analysed in this study. Smaller white markers correspond to abrasions without any detected stoichiometric olivine. During the crater floor campaign, the rover traversed the boundary between the Máaz and Séítah formations.

During the crater floor campaign, observations of the Máaz formation (abrasion targets: Guillaumes, Bellegarde, Montpezat and Alfalfa) revealed interlocking submillimetric to millimetric plagioclase and pyroxene, in addition to olivine altered to Fe-rich serpentine, interpreted as a lava flow that underwent aqueous alteration[24,43–47]. In the Séítah formation (abrasion targets: Garde, Dourbes and Quartier), coarse-grained pyroxene enclosing mm-scale olivine grains was interpreted as an igneous cumulate that later underwent aqueous alteration[20,26,43]. Olivine Fo-content values between 47 and 73 from PIXL and SuperCam data are consistent with chemical disequilibrium between olivine and the melt, further supporting the cumulate interpretation[20,40,48]. Recent investigations suggest that Quartier represents an evolution of the igneous body (Séítah formation) that was intruded as a shallow sill between lava flows of the Séítah and Máaz formations rather than being a member of the Séítah formation[49].

The upper fan campaign includes the Tenby and Otis Peak formations. The Tenby formation (abrasion targets: Solva, Solitude Lake) consists of medium-grained mafic sandstone with possible Fe-Mg carbonate cements[50]. The overlying conglomeritic Otis Peak formation (abrasion targets: Ouzel Falls, Gabletop Mountain, and Thunderbolt Peak) hosts millimetric clasts of olivine modified by a suite of alteration phases[51], and sandstones with sedimentary structures consistent with fluvial deposition[38,50]. Throughout both the fan front and upper fan campaigns, SuperCam detected a wide spread of olivine compositions (Fo-content: 52–78)[40].

A suite of compositionally distinct float boulders lies atop the Otis Peak formation; their origin and transport mechanism(s) to their present location are not clear. Two classes of boulders have been described[52]: (1) Olivine-rich, exemplified by the Falcon Lake boulder (abrasion target: Lake Haiyaha), which contains mm-scale olivine grains in textures reminiscent of an igneous cumulate[53,54]; and (2) Pyroxene-rich, exemplified by the Mount Meeker boulder (abrasion target: Dragon's Egg), which is notably rich in aluminous low-Ca-pyroxene[55]. PIXL results indicate that olivine in the olivine-rich boulders is far more magnesian (Fo-content between 70 and 80)[54] than other targets, while both PIXL and SuperCam results show a narrower compositional spread than other targets, consistent with a distinct, potentially more primitive source[40,53,54].

At Mandu Wall, *Perseverance* crossed a contact between the Margin Unit and the western sedimentary fan, which overlies it[39]. The Amherst Point abrasion target in the Hans Amundsen Memorial workspace in the eastern portion of the Margin Unit showed millimetric olivine grains variably altered to carbonate and rimmed by a low-Fe-Mg silicate, and intergranular space predominantly filled with Fe/Mg carbonate and silica[56–58]. *Perseverance* investigated an additional olivine-bearing abrasion target (Bill's Bay) of broadly similar texture and composition, before moving from the Eastern to Western Margin Unit. Two abrasions were created in the Western Margin Unit: Castle Geyser and Old Faithful Geyser. SuperCam results from the Margin Unit show a similar Fo-content range to the Séítah formation and to results from the fan front and upper fan campaigns[40].

Results and discussion

Monocrystalline olivine chemistry

The MIST algorithm[33] can be used to accurately measure and map the Fo-content of olivine in PIXL scans (Fig. 2a)[59]. Beam mixing[26,31], however, can result in contaminated Fo-content calculations. To reduce this effect, we used PIXL diffraction data (Fig. 2b) and extended the diffraction mapping technique developed by Orenstein et al.[23] to create constrained spatially coherent monocrystalline regions (Fig. 2c) that isolate individual crystals. Combining these monocrystalline regions with data from the MIST algorithm ensures that only olivine detected within these discrete mineral crystals is included in the analysis. This results in spatially mapped Fo-content from within individual mineral grains with reduced contamination from surrounding minerals (Fig. 2d). Comparison with context images (Fig. 2e, f) highlights the difficulty in identifying individual grains from images alone. Individual beam locations in the monocrystalline olivine maps (Fig. 2d) arise from one of two scenarios: (i) where olivine was identified in a single beam location within a larger monocrystalline region or (ii) where only one beam location remains after the monocrystalline region was spatially constrained. Using this method, monocrystalline olivine was identified in the crater floor, upper fan, and Margin Unit campaigns. No monocrystalline olivine was detected in the Máaz formation of the crater floor[60] or in the Shenandoah formation of the fan front (see Supplementary Notes). Table 1 and Table S1 show summary statistics for olivine detections.

Monocrystalline olivine was plotted on a sina plot[61,62], which shows the distribution of data by plotting individual data points with a width proportional to the density of points. Inspection of the sina plot of monocrystalline olivine regions reveals several distinct chemical populations encountered across the entire traverse (Fig. 3). Dourbes and Quartier (crater floor[34]; Fig. S3, S4), together with Lake Haiyaha (representing a boulder in float in the upper fan[54]; Fig. S8), all have a narrow distribution of Fo-content (low standard deviations), with Quartier the most fayalitic and Lake Haiyaha the most forsteritic population investigated here. The upper fan abrasion targets represent the greatest Fo-content distributions, with the Hartigan's dip test of unimodality[63] revealing evidence of multiple Fo populations in Gabletop Mountain and Thunderbolt Peak with modal centres at Fo-content of 52.3, 57.6, and 65.7/64.8 (Figs. 3 and S2, S9, S10, Tables S2, S3) representing distinct clusters of adjacent beam locations with similar Fo-content. Qualitatively, three distinct groupings can also be seen in Solva's Fo-content distribution, which similarly correspond to different clasts in the mapped area (Fig. S4). In the Margin Unit, Amherst Point, Bill's Bay, Castle Geyser, and Old Faithful Geyser have similar Fo-content distributions. A lithological distinction between the eastern and western regions of the Margin Unit[64–66] is not supported from SuperCam elemental and textural analyses[67] or by similar Fo-content values reported here (east mean = 51.2, SD = 3.1; west mean = 54.4, SD = 3.6), however a slight trend towards higher Fo-content is observed from east to west, possibly indicating a different alteration history related to increasing elevation from east to west.

Comparison to SuperCam LIBS

PIXL and SuperCam have detected olivine throughout *Perseverance's* traverse (see section "*Perseverance's* traverse"). Fo-content analysis from the two instruments often results in some discrepancies[48]. SuperCam overestimates Fo-content by ~3 for the olivine standard in their calibration suite due to underestimation of FeO_T and overestimation of SiO_2, causing some olivine to be incorrectly classified[48]. PIXL has quantification uncertainties for the olivine containing oxides (FeO_T, MgO, SiO_2) of up to 5%, leading to similar Fo-content uncertainties[68]. For example, SuperCam analyses give a Fo-content for Séítah olivine between 58 and 63[48], whereas, previous PIXL results of individual olivine grains reported a Fo-content of 55±1[20].

Analysis of the spatially resolved olivine data (Fig. 2, S3-S14) shows that olivine is not typically found in large areas but found in relatively small grains under 1 mm in length. The relatively small beam size of PIXL combined with contiguous mapping, allows us to isolate these individual grains using the combination of elemental and structural information and then to discard the edges of the grains, reducing the influence from the surrounding material. This type of analysis is not possible without contiguous mapping capabilities. SuperCam LIBS analyses are not contiguous, and therefore, individual grains cannot be isolated for analysis. Furthermore, the SuperCam beam is approximately twice the size of the PIXL beam[16,18], increasing the likelihood of contamination from the surrounding material. In the case of the Lake Haiyaha abrasion target (Fig. S8), both PIXL and SuperCam provide similar Fo-content values on a relatively large continuous olivine grain[40,53,54]. Therefore, we interpret that discrepancies in Fo-content between PIXL and SuperCam are largely due to beam mixing effects and different analysis regions (e.g., Fig. S3, S8), with quantification uncertainties playing a minor role.

Primary igneous versus sedimentary clastic olivine

The Dourbes and Quartier abrasion targets on the crater floor yield tightly distributed Fo-content populations (SD = 1.3, 1.4), consistent with in-place

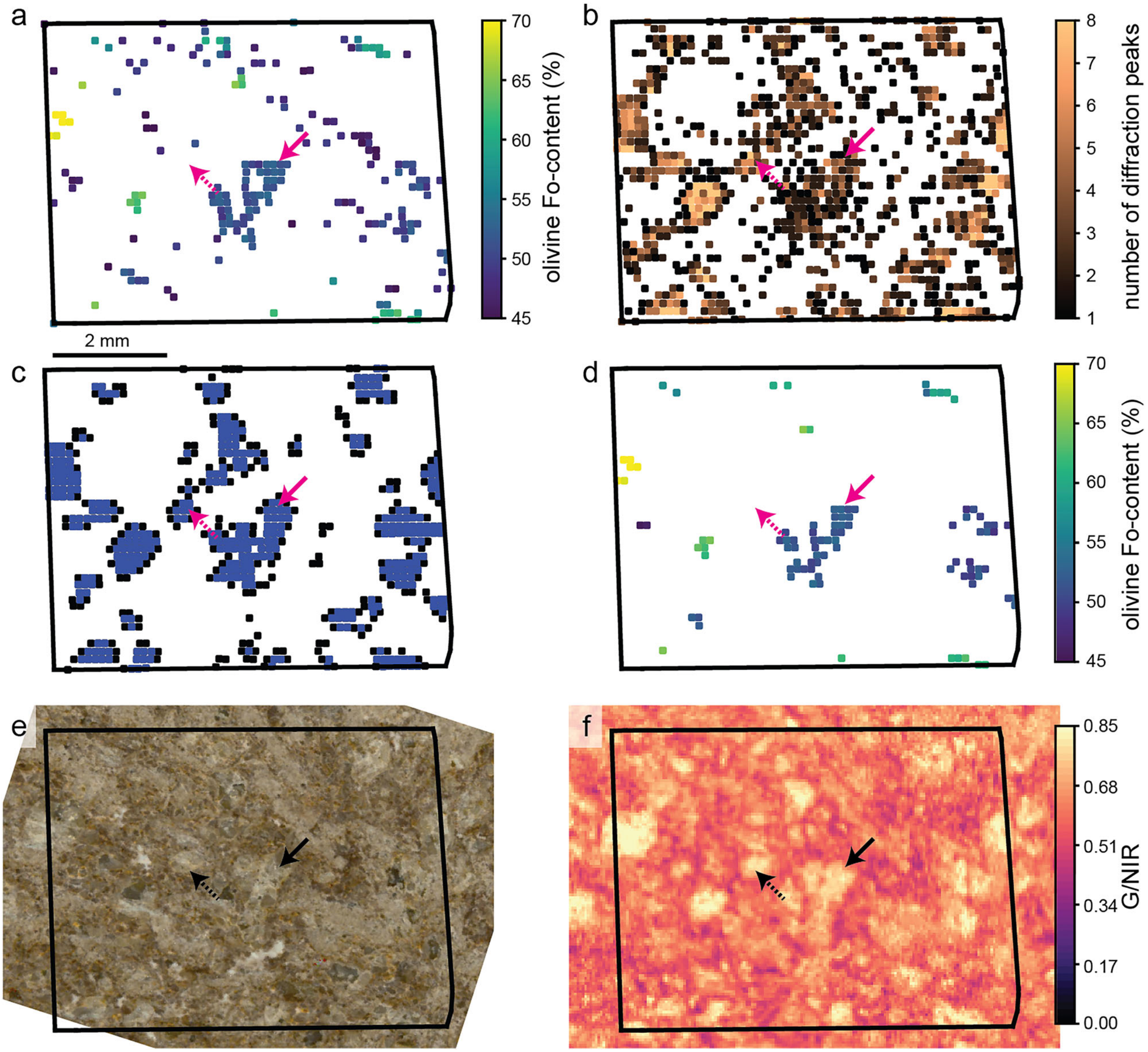

Fig. 2 | Combining MIST stoichiometic olivine and spatially coherent monocrystalline mapping to remove beam mixing effects and increase the Fo-content accuracy. a PIXL beam locations for a PIXL scan on the Solva abrasion patch (Figs. 1, 4c and S5) with compositions of stoichiometric olivine, as identified with the MIST algorithm[33,59]. Arrows point to a large olivine grain discernable in context imagery. **b** The number of diffraction peaks detected at each beam location. **c** Spatially coherent monocrystalline regions (black) and their spatially constrained interior regions (blue). **d** Compositions of monocrystalline stoichiometric olivine in the spatially constrained monocrystalline regions, as calculated with the MIST algorithm. **e** PIXL scan outline overlaid on a colourized ACI image[82] of the abrasion patch. Colourization image processing credit: NASA/JPL-Caltech/MSSS/S. Sharma. **f** PIXL MCC Green (530 nm)/IR (735 nm) image[83].

igneous cumulates that cooled from a single melt[20,49,69]. Similarly, we observed a very tight Fo-content distribution (SD = 1.3) in the Falcon Lake boulder (Lake Haiyaha abrasion target) with most olivine contained within large crystals (Fig. S8)[59].

In contrast to the tight Fo-content distributions of the olivine cumulates, the abrasion targets of the clastic upper fan likely represent multiple chemically distinct olivine sources. As determined from the Gaussian mixing model (supplementary material), the most forsteritic populations for these two upper fan abrasion targets have modal Fo-content values of 65.7 and 64.8, respectively (Table S2). This is significantly higher than the Fo-content of the crater floor, suggesting a different source, possibly the forsteritic olivine- and carbonate-rich western watershed[2,4,12,70] which fed Jezero crater via Neretva Vallis. As *Perseverance* traverses out of Jezero crater, it may encounter the sources of high Fo-content olivine for the clastic rocks and float boulders examined in the upper fan.

Compared to the upper fan, the relatively narrow spread of Fo-content in the Margin Unit olivine indicates less chemical diversity, indicating that if the Margin Unit is sedimentary, it was sourced from different material than the upper fan. The unimodal distribution of Margin Unit Fo-content populations (Table S2; mean = 52.19, SD = 3.57) closely resembles the Dourbes igneous cumulate (mean = 53.46, SD = 1.29), suggesting similar igneous origins, possibly from a shared magmatic event. The greater spread of Margin Unit Fo-content compared to Dourbes could be explained by (i) zonation effects, (ii) an increased contribution of fluorescence from additional phases[26,31], (iii) post emplacement alteration, and/or (iv) primary chemical heterogeneity in a melt.

Zonation of olivine crystals can increase Fo-content spreads. In olivine-phyric shergottites, Fe-Mg zonation is mostly seen as 100–200 micron thin, Fe-rich rims around mm-sized, more Mg-rich homogenous cores (e.g.,[71,72].). We found no clear evidence for zonation in the monocrystalline olivine

Table 1 | Olivine distributions within spatially constrained coherent monocrystalline regions and all MIST identified olivine for the abrasion targets with MIST identified olivine up to mission sol 1153

Campaign (formation/ unit)	Abrasion target (total no. of beam locations)	Spatially coherent olivine			MIST identified olivine		
		Range olivine Fo-content (%)	Mean (SD) olivine Fo-content (%)	No. beam locations (% of all beam locations)	Range olivine Fo-content (%)	Mean (SD) olivine Fo-content (%)	No. beam locations
Crater floor (Séítah)	Dourbes (5670)	43.56–58.06	53.46(1.29)	1435 (25.3%)	43.56–58.06	53.41(1.37)	1621
Crater floor (Séítah)	Quartier (6582)	37.75–48.07	45.48(1.32)	157 (2.4%)	36.75–48.07	44.79(2.29)	251
Crater floor (Máaz)	Montpezat[a] (2337)	-	-	0 (–)	15.69–20.96	19.02(2.90)	3
Upper fan (Tenby)	Solva (5670)	44.02–71.68	55.35(6.58)	149 (2.6%)	42.19–71.68	52.41(6.25)	349
Upper fan (Tenby)	Solitude Lake (2337)	58.91–62.63	61.01(1.12)	9 (0.5%)	45.03–62.63	52.73(3.96)	75
Upper fan (Otis Peak)	Ouzel Falls (5670)	49.49–68.96	60.09(5.62)	22 (0.4%)	32.34–68.96	60.14(6.71)	81
Upper fan (N/A)	Lake Haiyaha[b] (5188)	66.44–78.86	74.47(1.30)	1932 (37.3%)	54.55–78.86	74.33(1.53)	2259
Upper fan (Otis Peak)	Gabletop Mountain (5188)	51.07–68.74	59.92(6.68)	19 (0.4%)	41.43–68.74	52.70(6.11)	108
Upper fan (Otis Peak)	Thunderbolt Peak (2581)	49.60–65.77	57.77(5.07)	33 (1.3%)	35.47–68.15	55.29(6.37)	92
Margin (Margin)	Amherst Point (4674)	42.57–56.92	50.76(2.48)	257 (5.5%)	31.74–58.07	49.66(3.29)	533
Margin (Margin)	Bill's Bay (4674)	41.33–58.99	53.70(4.53)	50 (1.1%)	26.40–64.20	50.60(6.35)	160
Margin (Margin)	Castle Geyser (6666)	45.06–57.22	52.56(2.68)	71 (1.1%)	43.73–60.94	51.68(3.05)	372
Margin (Margin)	Old Faithful Geyser (2581)	47.61–60.53	56.36(3.52)	64 (2.5%)	44.23–62.48	54.59(3.59)	196

[a] Indicates no olivine in spatially constrained coherent monocrystalline regions identified in the abrasion.

[b] Denotes the abrasion was on a boulder.

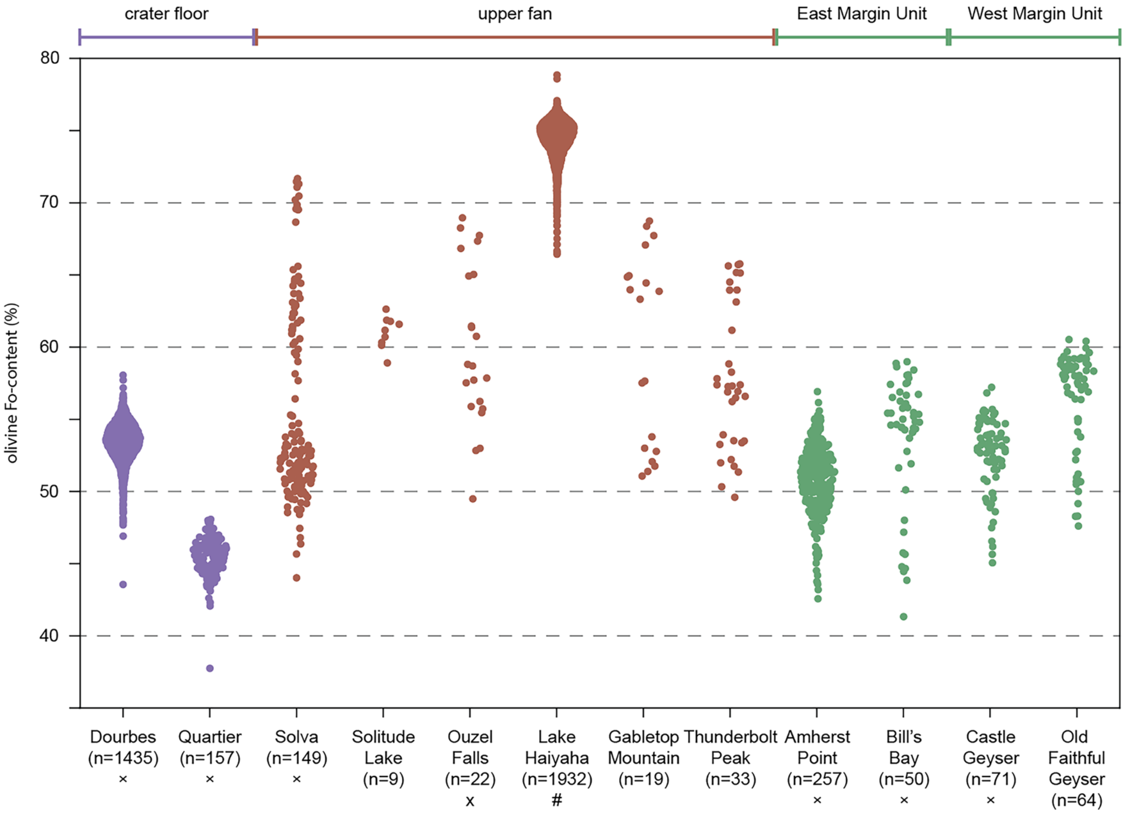

Fig. 3 | The forsterite content (Fo-content) for MIST olivine beam locations contained within spatially constrained coherent monocrystalline regions by abrasion target. # Indicates abrasions created on a boulder, and × corresponds to abrasion targets where a core sample was collected for Mars Sample Return.

regions studied (Figs. S3–S14) and by analogy with shergottite 'megacrysts', the signals analysed by PIXL would be dominated by core regions. Due to the strict MIST requirements for olivine identification[33] and because the edges of the monocrystalline regions were constrained to reduce the fluorescence contribution from additional phases (Fig. 2), we conclude that beam mixing effects are unlikely to be the cause of the increased Fo-content diversity in the Margin Unit.

Preferential dissolution of low Fo-content olivine, predicted by modelling performed under Martian surface conditions[73], can result in a shift towards higher overall Fo-content with less low Fo-content olivine, seen most clearly in the long tails towards low Fo-content in Bill's Bay and Old Faithful Geyser (Fig. 3). Further alteration of high Fo-content olivine results in silica-rich phases and clay phases[74], which would no longer meet the requirements for MIST identification[33]. Therefore, we suggest that olivine in the Margin Unit likely originates from a single igneous source, similar to the Dourbes abrasion target on the crater floor, but which has experienced a greater degree of aqueous alteration. These observations, in combination with the results from the Hartigan's dip test of unimodality, suggest that the variation in Fo-content in the upper fan is more likely to represent multiple sources of olivine rather than an aqueously altered olivine from a single source.

Using our novel technique combining spatial and chemical information, we are able to identify distinct chemical populations of olivine with less uncertainty than chemical data alone, allowing for inferences to be made concerning origin and emplacement. We find that in the igneous crater floor and in the sedimentary upper fan, Fo-content variations are consistent with the differing emplacement mechanisms proposed for these units. The results presented here indicate that the analysed portions of the Margin Unit likely represent an altered igneous cumulate rather than being sedimentary.

Methods

Creating spatially coherent monocrystalline regions

Diffraction peaks identified in PIXL spectra using a *t*-test across the count values in each of PIXL's two detectors, for every energy, result in a list of diffraction peaks at energies that can be visualised on an abrasion patch as beam locations containing diffraction[75] (Fig. 2b). The diffraction is partitioned into monocrystalline regions using the energy-dispersive Bragg equation and PIXL's beam geometry[23].

Monocrystalline regions are grouped in energy but do not incorporate spatial information[23]. Therefore, to interrogate spatially coherent single crystals, spatial information needs to be incorporated, which we implement in the following steps. Firstly, for each beam location, the distance to its eight nearest neighbours is calculated. For a perfect grid, this encompasses the closest beam locations in the orthogonal and diagonal directions. To filter out spatially incoherent beam locations (i.e., diffraction that is isolated to one beam location), we remove all beam locations that are not adjacent to at least two out of the nearest eight neighbours. The smallest monocrystalline region is therefore three beam locations. If the energy dependent beam size[76] is more than 1.5 times the average map spacing, then the minimum size for a monocrystalline region is increased to four. All beam locations contained

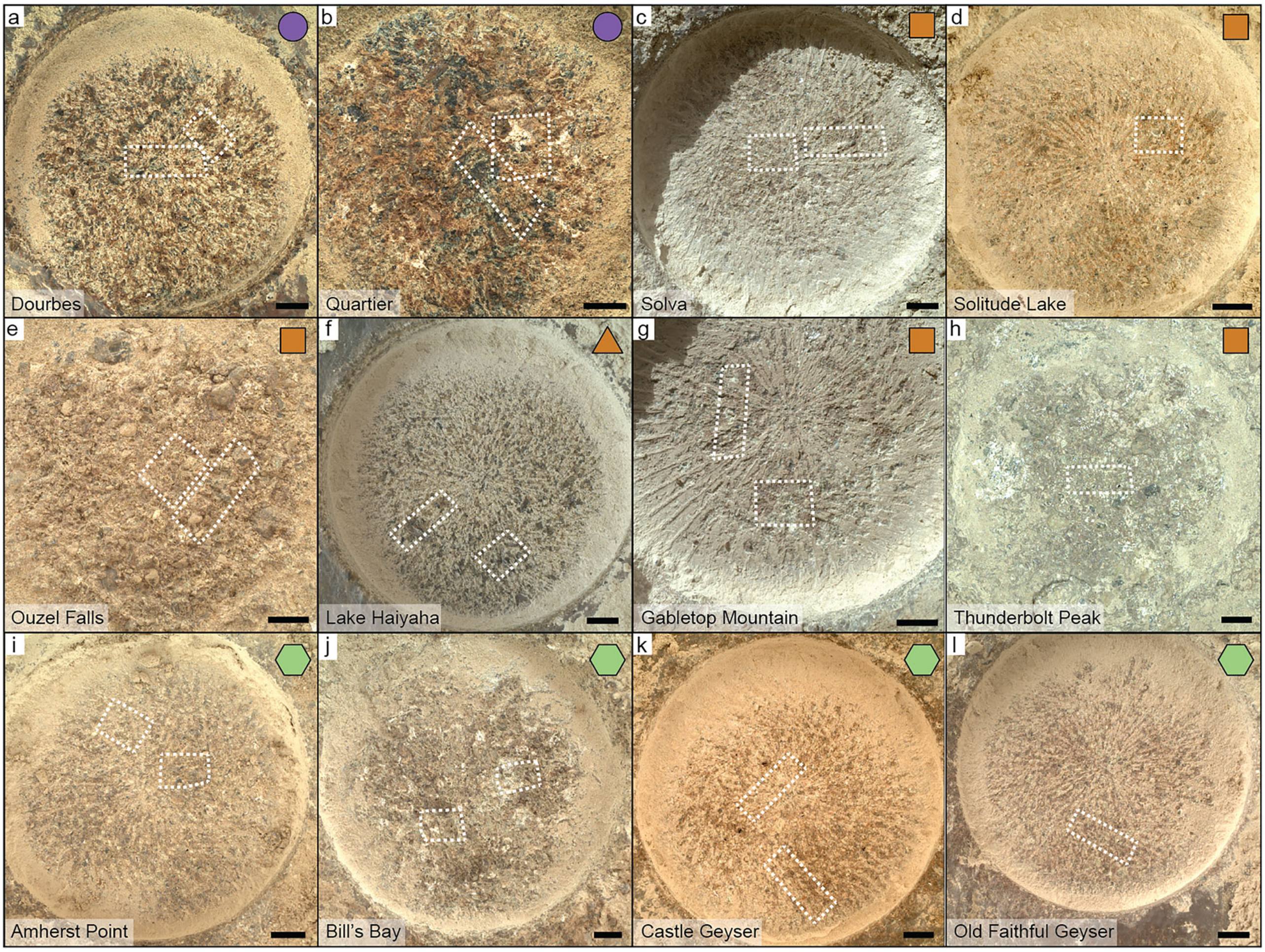

Fig. 4 | WATSON images of abrasion patches with PIXL scan footprints in dashed white areas for the scans included in this study. **a** = Dourbes, **b** = Quartier, **c** = Solva, **d** = Solitude Lake, **e** = Ouzel Falls, **f** = Lake Haiyaha, **g** = Gabletop Mountain, **h** = Thunderbolt Peak, **i** = Amherst Point, **j** = Bill's Bay, **k** = Castle Geyser, **l** = Old Faithful Geyser. Scalebar in each panel is approximately 5 mm. Coloured markers in the upper right of each panel correspond to the campaign location in Fig. 1. See Table S4 for image sources.

within overlapping spatially coherent monocrystalline regions were then flattened through energy space. To reduce beam mixing effects[26,31] semi-isolated beam locations at the edges of each coherent monocrystalline region where a beam location did not have three of the four nearest neighbours (Fig. 2c, black), contained within the spatially coherent monocrystalline region, were removed, leaving the spatially constrained interiors (Fig. 2c, blue). Three of the four nearest neighbours were selected, as any less than three increases the likelihood of regions outside of the monocrystalline region being included in the analysis.

Stoichiometric filtering for olivine

The Mineral Identification by SToichiometry (MIST) algorithm is a rules-based classification model used to identify mineral endmembers in high-resolution geochemical data[33]. MIST can identify minerals where the surface exposure is larger than PIXL's energy dependent X-ray spot size of ~120 µm (measured at ~8 keV[18,76]) and is ideally implemented on data representing single mineral phases[59], such as the monocrystalline regions reported here. The MIST algorithm is able to detect olivine with high confidence across all data considered here[59].

Beam locations were obtained from PIXLISE[75] (an open source software tool for visualising PIXL data) for areas identified by MIST as stoichiometric olivine endmembers, forsterite or fayalite. MIST uses normalised elemental data, so prior to inputting PIXL data into MIST, locations with oxide totals of less than 85% were excluded from the analysis, as these beam locations may contain significant amounts of non-quantified elements present below PIXL's detectable limit[26]. Instrument effects can also cause overestimation of elemental abundances[68,77], and so beam locations with oxide totals of greater than 105% were also removed from the analysis. Of the total MIST stoichiometric olivine, 4.3% has quantified totals outside this range. Of the MIST stoichiometric olivine within spatially coherent monocrystalline regions, 1.1% of beam locations had quantified totals outside of this range, consisting of 0.1% of crater floor beam locations, 3.3% of upper fan beam locations, 5.9% of Margin Unit beam locations, and 0.5% in the Lake Haiyaha boulder. Remaining spatially coherent monocrystalline regions containing MIST olivine were then selected for analysis (Fig. 2d).

MIST was given oxide abundances corrected for the effects of diffraction and surface roughness using PIXLISE v4 expressions[24], before the abundances were normalised and the olivine forsterite content was calculated. The MIST results here have also had any SO_3 and Cl determined to be allochthonous to the rock (i.e., from dust)[78–80] removed before normalisation[59]. We display the Fo-content per abrasion patch as a sina plot[61,62] in Fig. 3, allowing for a visual representation of the olivine distribution and density for each target.

Image registration

MCC, ACI, WATSON, and RMI images were aligned with an affine transform in a multi-stage control point image registration routine implemented in MATLAB[81]. In the first stage, three or more large features were selected to obtain the approximate relative orientation of the images. Subsequent stages focused on smaller features, with an increasing number of control points. At least five control points were used in the final stage.

Data availability

Data available at the NASA Planetary Data System https://pds.nasa.gov/.

Code availability

Code used in this manuscript is available at https://github.com/bjorens/PIXL_spatially_coherent_monocrystalline_regions/.

Received: 2 May 2025; Accepted: 16 January 2026;

References

1. Werner, S. C. The early martian evolution—constraints from basin formation ages. *Icarus* **195**, 45–60 (2008).
2. Hoefen, T. M. et al. Discovery of olivine in the Nilos Fossae region of Mars. *Science* **302**, 627–630 (2003).
3. Hamilton, V. E. & Christensen, P. R. Evidence for extensive, olivine-rich bedrock on Mars. *Geology* **33**, 433–436 (2005).
4. Ehlmann, B. L. et al. Orbital identification of carbonate-bearing rocks on Mars. *Science* **322**, 1828–1832 (2008).
5. Mustard, J. F. et al. Mineralogy of the nili fossae region with OMEGA/Mars Express data: 1. Ancient impact melt in the Isidis Basin and implications for the transition from the Noachian to Hesperian. *J. Geophys. Res. Planets* **112**, E8 (2007).
6. Mustard, J. F. et al. Composition, morphology, and stratigraphy of Noachian Crust around the Isidis basin. *J. Geophys. Res. Planets* **114**, E2 (2009).
7. Tornabene, L. L. et al. Surface and crater-exposed lithologic units of the Isidis Basin as mapped by coanalysis of THEMIS and TES derived data products. *J. Geophys. Res. Planets* **113**, E10 (2008).
8. Rogers, A. D., Warner, N. H., Golombek, M. P., Head, J. W. III & Cowart, J. C. Areally extensive surface bedrock exposures on Mars: many are clastic rocks, not lavas. *Geophys. Res. Lett.* **45**, 1767–1777 (2018).
9. Kremer, C. H., Mustard, J. F. & Bramble, M. S. A widespread olivine-rich ash deposit on Mars. *Geology* **47**, 677–681 (2019).
10. Ruff, S. W., Hamilton, V. E., Rogers, A. D., Edwards, C. S. & Horgan, B. H. N. Olivine and carbonate-rich bedrock in Gusev crater and the Nili Fossae region of Mars may be altered ignimbrite deposits. *Icarus* **380**, 114974 (2022).
11. Brown, A. J., Viviano, C. E. & Goudge, T. A. Olivine-carbonate mineralogy of the Jezero crater region. *J. Geophys. Res. Planets* **125**, e2019JE006011 (2020).
12. Goudge, T. A., Mustard, J. F., Head, J. W., Fassett, C. I. & Wiseman, S. M. Assessing the mineralogy of the watershed and fan deposits of the Jezero crater paleolake system, Mars. *J. Geophys. Res. Planets* **120**, 775–808 (2015).
13. Tarnas, J. D. et al. Characteristics, origins, and biosignature preservation potential of carbonate-bearing rocks within and outside of jezero crater. *J. Geophys. Res. Planets* **126**, e2021JE006898 (2021).
14. Viviano, C. E., Moersch, J. E. & McSween, H. Y. Implications for early hydrothermal environments on Mars through the spectral evidence for carbonation and chloritization reactions in the Nili Fossae region. *J. Geophys. Res. Planets* **118**, 1858–1872 (2013).
15. Horgan, B. H. N., Anderson, R. B., Dromart, G., Amador, E. S. & Rice, M. S. The mineral diversity of Jezero crater: evidence for possible lacustrine carbonates on Mars. *Icarus* **339**, 113526 (2020).
16. Maurice, S. et al. The SuperCam instrument suite on the Mars 2020 rover: science objectives and mast-unit description. *Space Sci. Rev.* **217**, 47 (2021).
17. Wiens, R. C. et al. The SuperCam instrument suite on the NASA Mars 2020 rover: body unit and combined system tests. *Space Sci. Rev.* **217**, 4 (2020).
18. Allwood, A. C. et al. PIXL: planetary instrument for X-ray lithochemistry. *Space Sci. Rev.* **216**, 134 (2020).
19. Moeller, R. C. et al. The Sampling and Caching Subsystem (SCS) for the scientific exploration of Jezero Crater by the Mars 2020 Perseverance rover. *Space Sci. Rev.* **217**, 5 (2020).
20. Liu, Y. et al. An olivine cumulate outcrop on the floor of Jezero crater, Mars. *Science* **377**, 1513–1519 (2022).
21. Schofield, R. E. et al. In *Lunar and Planetary Science XLVIII* 2955 (USRA, 2017).
22. Jones, M. W. M. et al. In situ crystallographic mapping constrains sulfate precipitation and timing in Jezero crater, Mars. *Sci. Adv.* **11**, eadt3048 (2025).
23. Orenstein, B. J. et al. In-situ mapping of monocrystalline regions on Mars. *Icarus* **420**, 116202 (2024).
24. Schmidt, M. E. et al. Diverse and highly differentiated lava suite in Jezero crater, Mars: constraints on intracrustal magmatism revealed by Mars 2020 PIXL. *Sci. Adv.* **11**, eadr2613 (2025).

25. Schrank, C. E., Jones, M. W. M., Howard, D. L., Berger, A. & Herwegh, M. Micro-scale structural and chemical characterisation of deformed rocks with simultaneous in-situ synchrotron X-ray fluorescence and backscatter diffraction mapping. *Chem. Geol.* **645**, 121886 (2024).
26. Tice, M. M. et al. Alteration history of Séitah formation rocks inferred by PIXL x-ray fluorescence, x-ray diffraction, and multispectral imaging on Mars. *Sci. Adv.* **8**, eabp9084 (2022).
27. Bhartia, R. et al. Perseverance's scanning habitable environments with Raman and luminescence for organics and chemicals (SHERLOC) investigation. *Space Sci. Rev.* **217**, 58 (2021).
28. Maki, J. N. et al. The Mars 2020 engineering cameras and microphone on the Perseverance rover: a next-generation imaging system for Mars exploration. *Space Sci. Rev.* **216**, 137 (2020).
29. Roeder, P. L. & Emslie, R. F. Olivine-liquid equilibrium. *Contrib. Mineral. Petrol.* **29**, 275–289 (1970).
30. Stöffler, D. & Knöll, H.-D. Research supported by the Deutsche Forschungsgemeinschaft. In *Proc. Lunar Science Conference*, *8th, Houston, Tex., March 14-18, 1977, Proceedings* 1849–1867 (Pergamon Press, Inc., 1977).
31. Kizovski, T. V. et al. Fe-phosphates in Jezero Crater as evidence for an ancient habitable environment on Mars. *Nat. Commun.* **16**, 6470 (2025).
32. Henley, T. L. J. *In Situ Investigation of the Martian Surface: Quantification of Dust Coverages in Gale Crater and Abrasion Marks in Jezero crater.* MSc thesis, Brock Univ. (2023).
33. Siebach, K. L., Moreland, E. L., Costin, G. & Jiang, Y. MIST: an online tool automating mineral identification by stoichiometry. *Comput. Geosci.* **206**, 106021 (2026).
34. Sun, V. Z. et al. Overview and results from the Mars 2020 Perseverance Rover's First Science Campaign on the Jezero Crater Floor. *J. Geophys. Res. Planets* **128**, e2022JE007613 (2023).
35. Stack, K. M. et al. Sedimentology and stratigraphy of the Shenandoah formation, western fan, Jezero crater, Mars. *J. Geophys. Res. Planets* **129**, e2023JE008187 (2024).
36. Herd, C. D. K. et al. Sampling Mars: Geologic context and preliminary characterization of samples collected by the NASA Mars 2020 Perseverance Rover Mission. *Proc. Natl. Acad. Sci. USA* **122**, e2404255121 (2025).
37. Huang, W. et al. Mineralogical diversity in the upper fan campaign at Jezero Crater, Mars. *J. Geophys. Res. Planets* **130**, e2024JE008750 (2025).
38. Nachon, M. et al. Overview of the Mars 2020 mission Perseverance rover third science campaign: exploring Jezero crater's upper fan. In *55th Lunar and Planetary Science Conference*. 2317 (https://www.hou.usra.edu/meetings/lpsc2024/pdf/2317.pdf, 2024).
39. Horgan, B. et al. Campaign overview and initial results from exploration of the Margin Unit in Jezero crater by the Perseverance rover. In *55th Lunar and Planetary Science Conference*. 2624. (https://www.hou.usra.edu/meetings/lpsc2024/pdf/2624.pdf, 2024).
40. Udry, A. et al. Igneous processes at Jezero Crater and comparison to other Martian igneous compositions. (https://www.hou.usra.edu/meetings/tenthmars2024/pdf/3052.pdf, 2024).
41. Udry, A. et al. What Martian Meteorites Reveal About the Interior and Surface of Mars. *J. Geophys. Res. Planets* **125**, e2020JE006523 (2020).
42. Rampe, E. B. et al. Mineralogy and geochemistry of sedimentary rocks and eolian sediments in Gale crater, Mars: a review after six Earth years of exploration with Curiosity. *Geochemistry* **80**, 125605 (2020).
43. Farley, K. A. et al. Aqueously altered igneous rocks sampled on the floor of Jezero crater, Mars. *Science* **377**, eabo2196 (2022).
44. Horgan, B. et al. Mineralogy, morphology, and emplacement history of the Maaz formation on the Jezero crater floor from orbital and rover observations. *J. Geophys. Res. Planets* **128**, e2022JE007612 (2023).
45. Udry, A. et al. A Mars 2020 Perseverance SuperCam Perspective on the Igneous Nature of the Máaz Formation at Jezero Crater and Link With Séítah, Mars. *J. Geophys. Res. Planets* **128**, e2022JE007440 (2023).
46. Wiens, R. C. et al. Compositionally and density stratified igneous terrain in Jezero crater, Mars. *Sci. Adv.* **8**, eabo3399 (2022).
47. Tosca, N. J. et al. In situ evidence for serpentinization within the Máaz formation, Jezero crater, Mars. *Sci. Adv.* **11**, eadr8793 (2025).
48. Beyssac, O. et al. Petrological traverse of the olivine cumulate séítah formation at jezero crater, Mars: a perspective from supercam onboard perseverance. *J. Geophys. Res. Planets* **128**, e2022JE007638 (2023).
49. Hernández-Montenegro, J. D. et al. Petrogenesis of the olivine cumulate outcrop Issole – The missing link between the Séítah and Máaz formations in Jezero crater, Mars. *Icarus* **437**, 116620 (2025).
50. Siebach, K. L. et al. PIXL analyses of sedimentary rocks in the Mars 2020 Perseverance upper fan campaign in Jezero crater. In *55th Lunar and Planetary Science Conference*. 2365 (https://www.hou.usra.edu/meetings/lpsc2024/pdf/2365.pdf, 2024).
51. Weiss, B. P. et al. Perseverance samples from the Jezero upper fan. In *55th Lunar and Planetary Science Conference* (https://www.hou.usra.edu/meetings/lpsc2024/pdf/1843.pdf, 2024).
52. Vaughan, A. F. et al. The boulder-rich blocky unit of the western jezero upper fan: discriminating olivine and pyroxene compositions and constraining provenance. *J. Geophys. Res. Planets* **130**, e2025JE009159 (2025).
53. Beyssac, O. et al. What are the olivine-rich boulders in the upper fan and Margin Unit at Jezero crater, Mars? In *55th Lunar and Planetary Science Conference (LPSC)*. (Lunar and Planetary Institute) (https://www.hou.usra.edu/meetings/lpsc2024/pdf/1493.pdf, 2024).
54. Moreland, E. L. et al. Falcon_Lake: an olivine-rich boulder in Jezero crater, Mars. In *55th Lunar and Planetary Science Conference*. 2030 (https://www.hou.usra.edu/meetings/lpsc2024/pdf/2030.pdf, 2024).
55. Treiman, A. H. et al. Mount_Meeker: a boulder of aluminous melt rock in Jezero crater, Mars. In *55th Lunar and Planetary Science Conference*. 1283 (https://www.hou.usra.edu/meetings/lpsc2024/pdf/1283.pdf, 2024).
56. Hurowitz, J. A. et al. PIXL results from Jezero crater's Margin Unit. In *55th Lunar and Planetary Science Conference*. 2541 (https://www.hou.usra.edu/meetings/lpsc2024/pdf/2541.pdf, 2024).
57. Garczynski, B. J. et al. Initial Mastcam-Z multispectral results from the Perseverance rover's exploration of the Margin Unit in Jezero crater, Mars. In *Proc. of the 55th Lunar and Planetary Science Conference*. (Woodlands: Lunar and Planetary Institute) (https://www.hou.usra.edu/meetings/lpsc2024/pdf/2708.pdf, 2024).
58. Sinclair, K. P., Catling, D. C. & Elam, W. T. Formation conditions of hydrated carbonates in the Margin Unit of Jezero crater examined by PIXL. In *Tenth International Conference on Mars*. 3434 (https://www.hou.usra.edu/meetings/tenthmars2024/pdf/3434.pdf, 2024).
59. Moreland, E. L. et al. Multiple episodes of fluid alteration in Jezero crater indicated by MIST mineral identifications in PIXL XRF data from the first 1100 sols of the Mars 2020 mission. *J. Geophys. Res. Planets* **130**, e2024JE008797 (2025).
60. Mandon, L. et al. Reflectance of Jezero Crater Floor: 2. Mineralogical Interpretation. *J. Geophys. Res. Planets* **128**, e2022JE007450 (2023).
61. seaborn_sinaplot (github, https://github.com/mparker2/seaborn_sinaplot, 2018).
62. sinaplot: an Enhanced Chart for Simple and Truthful Representation of Single Observations over Multiple Classes v. 1.1.0 (https://cran.r-project.org/web/packages/sinaplot/index.html, 2017).
63. Hartigan, J. A. & Hartigan, P. M. The dip test of unimodality. *Ann. Stat.* **13**, 70–84 (1985).
64. Horgan, B. et al. Exploration of carbonate-rich rocks in the Margin Unit by the Perseverance rover in Jezero crater. In *Tenth International Conference on Mars*. 3543 (https://www.hou.usra.edu/meetings/tenthmars2024/pdf/3543.pdf, 2024).

65. Jones, A. J. et al. Reconstructing the sedimentology and depositional setting of the Margin Unit, Jezero crater. In *55th Lunar and Planetary Science Conference*. 1994 (https://www.hou.usra.edu/meetings/lpsc2024/pdf/1994.pdf, 2024).
66. Randazzo, N. et al. Depositional hypotheses for the emplacement of the Margin Unit, Jezero crater, Mars. In *55th Lunar and Planetary Science Conference* 2108 https://www.hou.usra.edu/meetings/lpsc2024/pdf/2108.pdf, (The Woodlands, 2024).
67. Bedford, C. et al. Investigating the origin and alteration history of the margin unit in Jezero crater, Mars, with the SuperCam instrument. *LPI Contrib.* **3090**, 1946 (2025).
68. Heirwegh, C. M., Elam, W. T., O'Neil, L. P., Sinclair, K. P. & Das, A. The focused beam X-ray fluorescence elemental quantification software package PIQUANT. *Spectrochim. Acta Part B At. Spectrosc.* **196**, 106520 (2022).
69. Treiman, A. H. et al. The brac/dourbes olivine-cumulate rock, séítah formation, Jezero crater floor, Mars: its parent magma, and relation to basalts of the máaz formation. *J. Geophys. Res. Planets* **130**, e2024JE008539 (2025).
70. Fassett, C. I. & Head, J. W. III Fluvial sedimentary deposits on Mars: ancient deltas in a crater lake in the Nili Fossae region. *Geophys. Res. Lett.* **32** (2005).
71. Barrat, J. A. et al. Petrology and chemistry of the Picritic Shergottite North West Africa 1068 (NWA 1068). *Geochim. Cosmochim. Acta* **66**, 3505–3518 (2002).
72. Basu Sarbadhikari, A., Day, J. M. D., Liu, Y., Rumble, D. & Taylor, L. A. Petrogenesis of olivine-phyric shergottite Larkman Nunatak 06319: implications for enriched components in martian basalts. *Geochim. Cosmochim. Acta* **73**, 2190–2214 (2009).
73. Stopar, J. D., Jeffrey Taylor, G., Hamilton, V. E. & Browning, L. Kinetic model of olivine dissolution and extent of aqueous alteration on Mars. *Geochim. Cosmochim. Acta* **70**, 6136–6152 (2006).
74. Dehouck, E. et al. Weathering of olivine under CO2 atmosphere: a martian perspective. *Geochim. Cosmochim. Acta* **135**, 170–189 (2014).
75. Wright, A. P., Nemere, P., Galvin, A., Chau, D. H. & Davidoff, S. In *Proc. 28th International Conference on Intelligent User Interfaces* 91–105 (Association for Computing Machinery, Sydney, NSW, Australia, 2023).
76. Das, A. et al. Energy dependence of x-ray beam size produced by polycapillary X-ray optics. *X-Ray Spectrometry* **54**, 203–213 (2024).
77. VanBommel, S. X-ray interrogation effects in APXS and PIXL. *Data. LPI Contrib.* **3007**, 3044 (2024).
78. Schmidt, M. E. et al. Geochemical diversity in first rocks examined by the Curiosity Rover in Gale Crater: evidence for and significance of an alkali and volatile-rich igneous source. *J. Geophys. Res. Planets* **119**, 64–81 (2014).
79. Siebach, K. L. et al. Sorting out compositional trends in sedimentary rocks of the Bradbury group (Aeolis Palus), Gale crater, Mars. *J. Geophys. Res. Planets* **122**, 295–328 (2017).
80. Stolper, E. M. et al. The petrochemistry of Jake_M: a martian mugearite. *Science* **341**, 1239463 (2013).
81. The MathWorks, Inc. MATLAB and Image Processing Toolbox Release 2023b. (The MathWorks, Inc., Natick, Massachusetts, United States, 2023).
82. Sharma, S. et al. Multi-instrument Image Correlation for In Situ Planetary Science on Mars 2020. In *Proc. IEEE Aerospace Conference* 1–13 https://doi.org/10.1109/AERO58975.2024.10521366 (IEEE, 2024).
83. Klevang, D. A. et al. Pre-flight geometric and optical calibration of the planetary instrument for X-ray lithochemistry (PIXL). *Space Sci. Rev.* **219**, 11 (2023).

Acknowledgements

This research was supported by Australian Research Council grant DE210100205. The research was carried out in part at the Jet Propulsion Laboratory, California Institute of Technology, under a contract with the National Aeronautics and Space Administration (80NM0018D0004). E.A.C. thanks the Natural Sciences and Engineering Research Council of Canada (grant #RGPIN-2023-03413) and the Canadian Space Agency (grant #22EXPCOI4) for their support. We acknowledge the members of the Mars 2020 team who performed mission operations and thank Christoph Schrank, Olivier Beyssac, Nicolas Mangold, Elise Clavé, and the SuperCam team for feedback that improved the manuscript. We also thank Jesper Henneke and David Arge Klevang for their assistance in aligning PIXL footprints to ACI and MCC images.

Author contributions

Brendan J. Orenstein contributed to conceptualization, methodology, software, formal analysis, investigation, writing—original draft, writing—review and editing, and visualization. David T. Flannery contributed to conceptualization, methodology, investigation, writing—original draft, writing—review and editing, visualization, supervision, and funding acquisition. Michael W. M. Jones contributed to conceptualization, methodology, software, formal analysis, investigation, writing— original draft, writing—review and editing, visualization, and supervision. Eleanor L. Moreland contributed to conceptualization, methodology, software, formal analysis, investigation, writing—original draft, writing—review and editing, and visualization. Kirsten L. Siebach contributed to conceptualization, methodology, software, formal analysis, investigation, writing—original draft, writing—review and editing, and supervision. Michael M. Tice contributed to methodology, software, and writing— review and editing. Allan H. Treiman contributed to methodology, investigation, writing—original draft, and writing—review and editing. Briony Horgan contributed to conceptualization, validation, investigation, writing—review and editing, and supervision. Balz Kamber contributed to conceptualization, methodology, investigation, supervision, and writing—review and editing. Athanasios Klidaras contributed to conceptualization, validation, investigation, and writing—review and editing. Luke Nothdurft contributed to conceptualization, methodology, investigation, writing—review and editing, and visualization. Yang Liu contributed to writing—original draft, writing—review and editing, and visualization. Edward Cloutis contributed to writing—original draft, and writing—review and editing. Abigail C. Allwood contributed to project administration, writing—review and editing, and funding acquisition. Scott VanBommel contributed to writing—review and editing.

Competing interests

The authors declare no competing interests.

Additional information

Supplementary information The online version contains supplementary material available at https://doi.org/10.1038/s43247-026-03227-2.

Correspondence and requests for materials should be addressed to David T. Flannery.

Peer review information *Communications Earth and Environment* thanks Elizabeth Rampe and the other, anonymous, reviewer(s) for their contribution to the peer review of this work. Primary Handling Editors: Ke Zhu and Joe Aslin. [A peer review file is available.]